


Consideration of Oblique Incidence in 3-D Imaging of a Planar Interface With a Circular Dipole Array in an Air-Filled Borehole

Satoshi Ebihara , Member, IEEE, Shyuhei Kotani, Kengo Fujiwara, Yuta Kimura, Takaaki Shimomura, and Ryota Uchimura

Abstract—We consider the effects of oblique incidence of a wave on the creation of a 3-D image of a planar interface with an array-type directional borehole radar. In this study, we focus on the situation where the radar probe is close to the planar interface. In such circumstances, the reflected wave from the planar interface may be incident on the receiving array antenna at very steep elevation angles. As a result, borehole effects cause differences in the arrival times of the wave at the array elements, and consequently some errors emerge in imaging the planar interface. Observing the arrival time differences, we present an algorithm to compensate those errors in creating a 3-D image of a planar interface. Computer simulations predict that the errors may occur when the circular dipole array antenna is in an air-filled borehole in rock. Numerical simulations show that our proposed algorithm generates a 3-D image of an interface around an exact position, whereas conventional methods produce some spurious images opposite to the correct position (i.e., out of position by 180°). We then applied the proposed method to analyze reflected waves from a real-world fault in rock. A 3-D image of the fault could be successfully created, which was not possible using the conventional method.

Index Terms—Critical elevation angle, dipole array antenna, directional borehole radar, oblique incidence, plane wave.

I. INTRODUCTION

THREE-DIMENSIONAL reconstruction of geological interfaces, faults, and fractures in rocks is essential for effective use of underground space. For constructing final disposal sites of high-level radioactive waste from nuclear power plants,

the locations of 3-D faults and fractures need to be known [1], [2]. One way is to drill boreholes to collect core samples, which can give geological information of the site. After drilling, several well loggings in the drilled hole may be performed. Another case may be investigation of the geological situation condition ahead of a tunnel face [3]. For this purpose, a borehole is drilled from a gallery in the direction of the tunnel. After the borehole is created, measurements are carried out inside the borehole.

Borehole radar measurement is a promising technique to image planar interfaces inside the borehole. Computer simulation results have shown that borehole radar may be able to estimate the orientation and location of water-filled fractures [4], and also monitor a reservoir in a smart well [5]. Field experiments have proved that a singlehole borehole radar can image water-filled fractures in rock and estimate the dip angle of the fractures [6]. The singlehole borehole radar can also produce good images of a cliff [7], [8]. Computer simulations have predicted that a singlehole borehole radar may also be able to detect a planar interface using guided waves along the borehole [9]. In addition, the singlehole borehole radar can image rock interfaces with energy flow domain reverse-time migration [10]. However, these studies were all carried out with an omnidirectional borehole radar for 2-D imaging of subsurface objects.

Directional borehole radar can also be used to estimate the 3-D locations of geological interfaces with a single borehole. Many authors have already proposed and tested directive antennas in a borehole. A possible directive antenna is a circular dipole array antenna in a borehole (CAB) [11]–[13]. The difference in arrival times of the signals received by the dipole elements leads to an estimation of the direction of arrival (DOA) of the received wave. The CAB can estimate the 3-D position of a subsurface tunnel [14], and generate a 3-D image of an interface in rock [15]. The algorithm for an Adcock direction-finding antenna may be applied to the CAB [14]. A linear prediction-based DOA estimator may also be employed for 3-D imaging with the CAB [16]. The directional borehole radar with CAB is now being used for commercial purposes [17].

In a borehole radar measurement, cylindrical layers, which constitute the medium inside the borehole, always exist around the antenna, sometimes significantly influencing the antenna

Manuscript received February 22, 2020; revised May 28, 2020; accepted June 10, 2020. Date of publication June 23, 2020; date of current version July 8, 2020. This work was supported by Japan Society for the Promotion of Science KAKENHI under Grant 18K05019. (Corresponding author: Satoshi Ebihara.)

Satoshi Ebihara is with the Department of Electrical and Electronic Engineering, Faculty of Engineering, Osaka Electro-Communication University, Neyagawa 572-8530, Japan (e-mail: s-ebihara@m.ieice.org).

Shyuhei Kotani is with Kurihara Kogyo Company, Ltd., Osaka 530-0017, Japan (e-mail: ee14a029@oecu.jp).

Kengo Fujiwara is with Mitsubishi Electric Building Techno Service Company, Ltd., Tokyo 100-0006, Japan (e-mail: ee14a073@oecu.jp).

Yuta Kimura is with Kinden Corporation, Osaka 531-8550, Japan (e-mail: ee09a040@oecu.jp).

Takaaki Shimomura is with West Nippon Expressway Engineering Kansai Company, Ltd., Ibaraki 567-0032, Japan (e-mail: ee09a045@oecu.jp).

Ryota Uchimura is with Kanden Engineering Corporation, Osaka 530-6691, Japan (e-mail: ee09a015@oecu.jp).

Digital Object Identifier 10.1109/JSTARS.2020.3004479

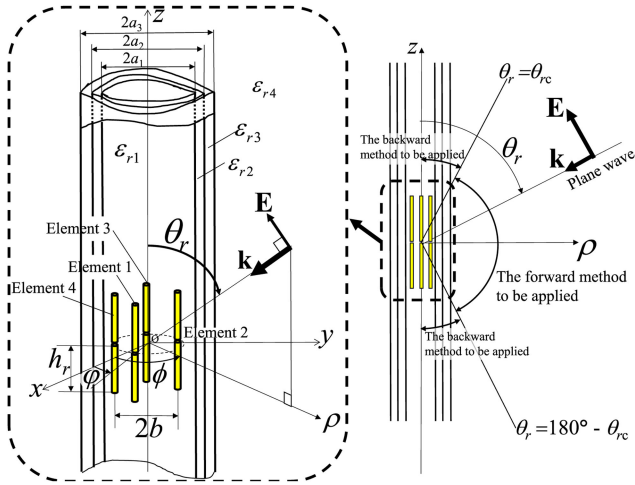


Fig. 1. Dipole array antenna in a borehole and the critical elevation angle. The value of ϵ_{r_i} is the relative complex permittivity in the i th layer.

characteristics and received radar signals [18], [19]. These variations caused by the borehole existence are sometimes called the borehole effect. We have recently established that particular phenomena occur in electromagnetic fields around the CAB [20]. When a plane wave is incident on the CAB at the critical elevation angle θ_{rc} (CEA), there is no difference in the arrival times measured by the dipole elements. Vertical and azimuthal electric field components on the cylindrical boundaries cause these phenomena to occur. They contribute to total electric fields around the antenna equally and cancel each other out. The order of arrival at the dipole elements at a steeper incident elevation angle than the CEA is opposite to that for normal incidence. In this case, the azimuthal component of the electric field on the cylindrical boundaries has a larger magnitude than the vertical one. This fact causes the difference in the arrival order between the normal and oblique incidence cases. Such phenomena should influence DOA estimation with the CAB. However, few authors have considered these phenomena in their 3-D estimation using the CAB.

In this article, we propose a 3-D imaging method of a planar interface close to a borehole using the CAB. In Section II, we review the antenna characteristics of the CAB, in relation to the CEA. In Section III, we formulate and analyze the situation where the CAB measures the planar interface. In Section IV, we propose a method to estimate 3-D imaging, considering the CEA. In Section V, numerical simulation results are presented, showing the validity of the proposed method. In Section VI, an experimental result using the proposed method for imaging a fault is presented.

II. DOA ESTIMATION WITH THE CAB

We review the CAB in this section. Fig. 1 shows the CAB antenna configuration. Dipole elements are arranged in a circle, and the azimuth angle φ represents the direction of the dipole element location. When a plane wave with elevation angle θ_r is incident on the CAB, the arrival times of the incoming wave

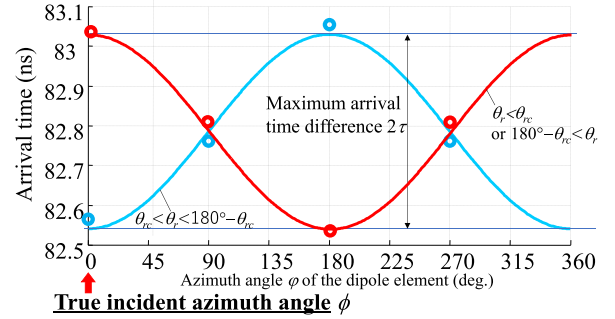


Fig. 2. Examples of fitting sine curves to the arrival times and estimation of the incident azimuth angle $\phi = 0^\circ$. The blue circles and curve are when the plane wave is incident almost normally, while the red ones are for the steep oblique incidence.

at the dipole elements can be measured, and the differences in the arrival times enable the estimation of the incident azimuth angle ϕ of the wave, referred to as DOA. Our great interest is estimation of the angle ϕ with the CAB signals. Fig. 2 shows examples of the arrival times versus the azimuth directions φ of the dipole elements. The circles denote the arrival times at the dipole elements, and the solid curve is a sine curve fitted with the least-squares method. We showed the two cases for both the almost normal and steep oblique incidences in the figure. The azimuth angle φ for the shortest arrival time is determined as the estimated azimuth angle ϕ in the case of the almost normal incidence, i.e., the blue circles and curve in the figure [20]. This procedure is referred to as the forward method in this article. In this method, we assume that the dipole array antenna is in homogeneous media, and the antenna element, which exists closest receives the wave first. Almost all authors in the past adopted this idea to estimate the DOA, although there were some differences in their procedures [14]–[16]. We define the maximum arrival time difference 2τ (MATD) as the difference between the longest and the shortest time. Note that the MATD depends on the elevation angle θ_r of the incident wave and $0 \leq 2t$.

The CEA θ_{rc} may be estimated numerically, as they did in [20]. The CEA is a borehole-specific value, determined by the medium around the antenna and the size of the borehole. The CEA has two values as θ_{rc} and $180^\circ - \theta_{rc}$ ($0^\circ < \theta_{rc} < 90^\circ$). When the elevation angle θ_r is θ_{rc} or $180^\circ - \theta_{rc}$, the MATD becomes very small, and the DOA cannot be estimated. The forward method may be applied when the wave is incident on the CAB in the range $\theta_{rc} < \theta_r < 180^\circ - \theta_{rc}$. When the elevation angle θ_r is in the range $\theta_r < \theta_{rc}$ or $180^\circ - \theta_{rc} < \theta_r$, which corresponds to the case of the red circles and curve in Fig. 2, the arrival order of the wave becomes opposite to the case of the almost normal incidence [20]. This fact suggests that the azimuth angle φ with the longest arrival time as derived from the fitted sine curve should be the estimated DOA when the wave is incident with the angles θ_r of $\theta_r < \theta_{rc}$ or $180^\circ - \theta_{rc} < \theta_r$. This estimation method is referred to as the backward method in this article.

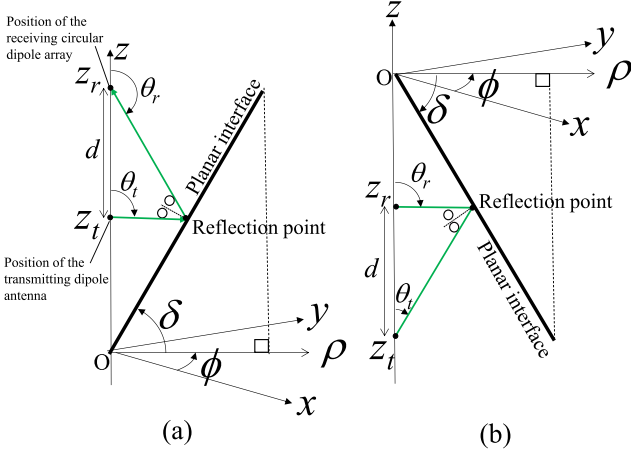


Fig. 3. Antenna positions and the planar interface. (a) Antennas are on the upper side of the planar interface in (a), while they are on the lower side of the interface in (b).

III. REFLECTION FROM A PLANAR INTERFACE

In this section, the problem that the CEA creates when the DOA of a planar interface with the CAB is estimated is formulated. First, it is essential to know the relationship between the antenna position and the elevation angle of the wave, which decides the occurrence of phenomena related to the CEA. The geometrical optics (GO) approximation [21], an approximate high-frequency method, is adopted.

A. Formulation

Consider the planar interface intersecting the z -axis at the origin O , as shown in Fig. 3. The interface is inclined by the dip angle δ ($0^\circ < \delta < 90^\circ$). There are a point transmitter and a point receiver at $z = z_t$ ($z_t < -d$ or $0 < z_t$) and $z = z_r$ ($z_r < 0$ or $d < z_r$) on the z -axis, respectively, where the positive real number d is the distance between the transmitter and the receiver, i.e., $z_r - z_t$. We assume the occurrence of specular reflection on the plane. The transmitter radiates a wave at the output elevation angle θ_t ($0 < \theta_t < 180^\circ$), and the reflected wave arrives at the incident elevation angle θ_r ($0 < \theta_r < 180^\circ$). Considering geometry, the tangent of the angle θ_i ($i = t$ or r) when the antennas are on the upper side of the planar interface is

$$\tan \theta_i = \frac{-2z_r \tan \delta (d - z_r)}{\tan^2 \delta \{2z_r^2 - 2(z_i + d)z_r + dz_i\} - 2z_i z_r + dz_i} \quad (d < z_i) \quad (1)$$

where if $i = t$, $\theta_i = \theta_t$ and $z_i = z_t$, whereas, if $i = r$, $\theta_i = \theta_r$ and $z_i = z_r$. Converting the variables in (1) as

$$\begin{cases} z_t \rightarrow -z_r \\ z_r \rightarrow -z_t \\ \theta_t \rightarrow 180^\circ - \theta_r \\ \theta_r \rightarrow 180^\circ - \theta_t \end{cases} \quad (2)$$

The tangent when the antennas are below the planar interface is

$$\tan \theta_i = \frac{-2z_t \tan \delta (d + z_t)}{\tan^2 \delta \{2z_t^2 - 2(z_i - d)z_t - dz_i\} - 2z_i z_t - dz_i} \quad (z_i < 0) \quad (3)$$

Since the inverse tangent is a multivalued function, the proper value should be chosen carefully to solve the angle θ_i in (1) and (3). Taking the limits of θ_i in (1) and (3), we get

$$\lim_{z_r \rightarrow \infty} \theta_i = 180^\circ - \delta \quad (4)$$

$$\lim_{z_r \rightarrow -\infty} \theta_i = \delta \quad (5)$$

$$\lim_{z_r \rightarrow +d} \theta_i = \begin{cases} 180^\circ - 2\delta, & (i = t) \\ 180^\circ, & (i = r) \end{cases} \quad (6)$$

and

$$\lim_{z_r \rightarrow -0} \theta_i = \begin{cases} 0^\circ, & (i = t) \\ 2\delta, & (i = r) \end{cases} \quad (7)$$

These limits are useful in drawing the graph of the elevation angles versus the antenna positions. The derivative of the functions $\tan \theta_r$ is

$$\frac{d}{dz_r} \tan \theta_r = \frac{-d \sin (2\delta)}{\{z_r + z_r \cos (2\delta) - d \cos (2\delta)\}^2} < 0. \quad (8)$$

This equation implies that the angle θ_r decreases monotonically when the value z_r ($> d$) increases, while the angle θ_r increases monotonically as the value of z_r (< 0) increases. According to the derivative

$$\frac{d}{dz_t} \tan \theta_t = \frac{d \sin (2\delta)}{\{z_t + z_t \cos (2\delta) + d \cos (2\delta)\}^2} > 0. \quad (9)$$

The angle θ_t increases monotonically when the value z_r ($> d$) increases, while the angle decreases monotonically as the value z_r (< 0) increases.

B. Analysis

We substitute some numerical values for the variables in (1) and (3) and obtain the solid and dotted black bold curves of the angles θ_i in Fig. 4. This figure shows the relationship between the antenna position and the elevation angles. In the figure, we find that if the transmitter position z_t approaches $+0$ and the value z_r approaches $d + 0$, then the elevation angle θ_r increases monotonically and converges to 180° at $z_r = d$. These results coincide with (6). Since choice in the forward method and backward method depends on the elevation angles in the estimation of the DOA with the CAB, the relationship between the elevation angle and the CEA is important. From now on in this article, we assume that only the receiver is a CAB, while the transmitter is an omnidirectional dipole antenna. The previous literatures [14], [12], [22], [16] on the CAB also adopted this assumption. It is to be noticed that similar conclusions may be obtained even if the transmitter is a CAB. In Fig. 4, we find that the CEA, $180^\circ - \theta_{rc}$, intersects the curve of θ_r at only one point

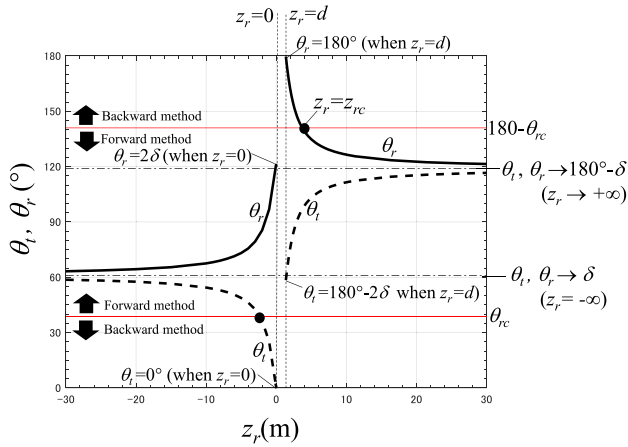


Fig. 4. Outgoing elevation angle θ_t , incident elevation angle θ_r , and the critical elevation angle θ_{rc} . We assumed $d = 1.36$ m, $\delta = 61^\circ$, and $\theta_{rc} = 39^\circ$ in this figure.

since the curve θ_{rc} increases monotonically, as shown in (8). Now, we define the critical receiver position z_{rc} (CRP) as the location where the reflected wave is incident on the receiver at CEA. Substituting $180^\circ - \theta_{rc}$ in (1), we define the CRP as

$$z_{rc} = \frac{d}{2} \cdot \frac{2 \tan \delta + \tan(180^\circ - \theta_{rc}) - \tan^2 \delta \tan(180^\circ - \theta_{rc})}{\tan \delta + \tan(180^\circ - \theta_{rc})} \quad (10)$$

$(d < z_{rc}).$

If the receiver is at $z_r > z_{rc}$, the elevation angle θ_r is at the range $\theta_{rc} < \theta_r < 180^\circ - \theta_{rc}$, and we should apply the forward method to estimate the DOA. In other positions such as $d < z_r < z_{rc}$, the backward method should be suitable for DOA estimation. When $z_r < 0$, we may apply the forward method to estimate the DOA since we can confirm $\theta_{rc} < \theta_r < 180^\circ - \theta_{rc}$ in the antenna positions shown in Fig. 4.

Note that the existence of the CRP depends on combinations of the values of θ_{rc} and δ , this ambiguity influences choice of the DOA estimation method. In Appendix A, we discuss the CRP existence on θ_{rc} δ plane. We give the example of numerical values of θ_{rc} in Appendix B. According to these results, we find that the existence of CRP would influence the planar interface measurement significantly, especially when we use the CAB in an air-filled borehole in rock.

IV. 3-D IMAGING ALGORITHM

We defined the origin in Fig. 3 as the intersection position between the z -axis and the interface. However, the intersection position is usually not known before the measurement. Furthermore, the vertical axis should be directed downward as it is used in the actual measurement. Now, we define the transformation formula between the D -axis and the z -axis as

$$z = D_0 - D \quad (11)$$

where the D -coordinate value is referred to as depth, and the origin of the D -axis may be at the entrance of the borehole. The

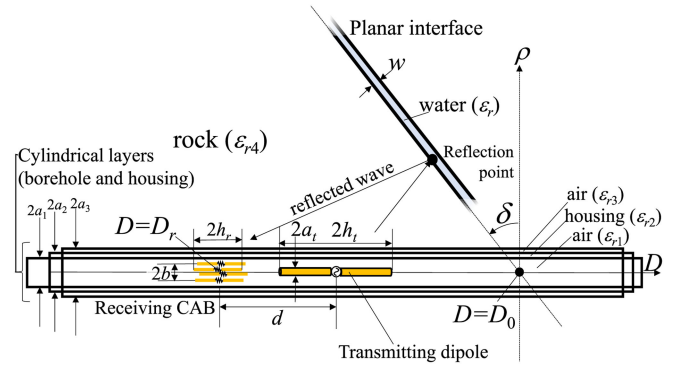


Fig. 5. Computer simulation model of the borehole radar measurement. The receiving CAB is at $D = D_r$ and the planar interface intersects with the D -axis at $D = D_0 = 35.2$ m. The parameters are $w = 0.5$ m, $\epsilon_r = 30 - j(2 \times 10^{-1} \text{ S/m})/(\epsilon_0 \omega)$, $2a_1 = 4.4$ cm, $2a_2 = 5.4$ cm, $2a_3 = 7.6$ cm, $\epsilon_{r1} = 1$, $\epsilon_{r2} = 5$, $\epsilon_{r3} = 1$, $\epsilon_{r4} = 15 - j(1 \times 10^{-2} \text{ S/m})/(\epsilon_0 \omega)$, $d = 1.36$ m, $2h_r = 20$ cm, $2b = 4$ cm, $2h_t = 1.34$ m, and $2a_t = 4.1$ cm.

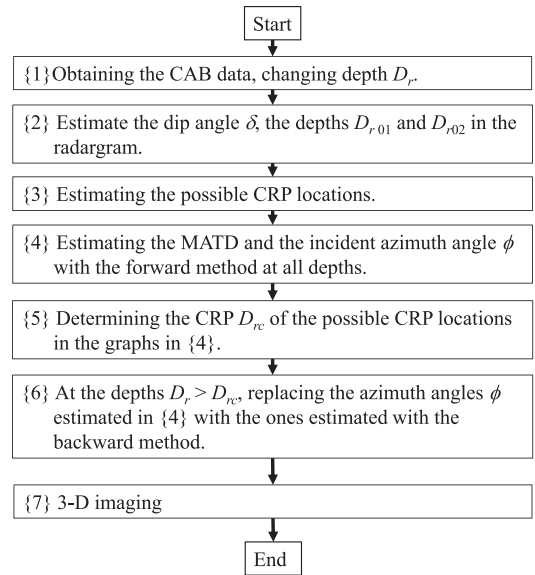


Fig. 6. Proposed 3-D imaging algorithm.

constant value D_0 represents the D -coordinate value, where the borehole intersects the planar interface. Substituting t , r , and rc for i in $z_i = D_0 - D_i$, we may define D_t , D_r , and D_{rc} of the transmitter, receiver, and CRP position in D coordinate, respectively. Fig. 5 shows the model of the borehole radar measurement of a planar interface with the CAB. The omnidirectional dipole antenna and the receiving CAB are in cylindrical layers, simulating the medium in a borehole. Planar layers are employed as a radar target. The scattered fields from the intersection $D = D_0$ are ignored.

In this section, we propose a 3-D imaging algorithm when the planar interface is close to the antennas. We assume that the antennas are on the left side of the planar interface, namely $D_r < D_0 - d - h_t$, as in Fig. 3(a), and the combination of the dip angle and the CEA belong to region 1 or 2 in Fig. 13. Fig. 6 shows all the procedures for the proposed algorithm. We assume that the

wave velocity in the outermost layer is known. For example, well logging with the singlehole borehole radar can be carried out to estimate the velocity [23]. We add the following comments for each procedure in the proposed algorithm.

- 1) We scan the radar probe with distance d fixed, and acquire the CAB signals at a constant interval.
- 2) We plot a radargram of the arrival time versus the depth D_r from the time domain signal obtained from one dipole element of the CAB. In this radargram, we choose the arrival time of a direct wave from the transmitter to the receiver. Also, we detect a reflected wave from the planar interface and draw two approximate lines representing the arrival times of the reflected waves. We choose the depth values D_r of intersections between the two drawn lines and the direct wave arrival time on the radargram plane, and then substitute the depth values for D_{r01} and D_{r02} ($D_{r01} < D_{r02}$). We estimate the dip angle δ of the planar interface from the slope of the approximate lines. In this estimation, (17) in Appendix C is useful.
- 3) We estimate the positions where the CRP may exist approximately. We name those positions the possible CRP locations with regards to the receiver position D_r satisfying

$$D_{r01} + d - z_{rc} \leq D_r \leq D_{r02} + d - z_{rc} \quad (12)$$

where we may estimate z_{rc} with (10), the CEA, which can be calculated theoretically from [20 (19)], and the dip angle estimated in 2).

- 4) We estimate the DOA of the reflected wave with the forward method, and the MATD at all receiver positions. We draw a graph of each DOA and MATD versus the receiver positions.
- 5) From the two graphs in 4), we determine the CRP, D_{rc} . This value may be estimated to be the receiver position where the estimated DOA rapidly changes, and the MATD becomes minimum.
- 6) We replace the DOA in 4) with the DOA estimated by the backward method at positions D_r deeper than D_{rc} , namely $D_{rc} < D_r$.
- 7) We apply the 3-D imaging algorithm proposed in [15] with the updated DOA in 6). We obtain the coordinates (ρ, ϕ, z) of the reflection points on the planar interface and the normal vectors \mathbf{n} to the planar interface.

V. NUMERICAL SIMULATION

A. CAB Signal Generation With MoM

We generate the CAB signal with the model in Fig. 5, which simulates a horizontal air-filled borehole drilled across a fault. We need to calculate the impedance matrix of the CAB with the method of moments (MoM) [20], [24]. Besides this, Green's functions of the reflected fields, which represent transmission from the transmitter to the receiver via the interface, should be considered. For this purpose, we need to calculate fields reflected from an interface when a z -directed Hertzian dipole in a cylindrical layer, which corresponds to (51) in Hansen's

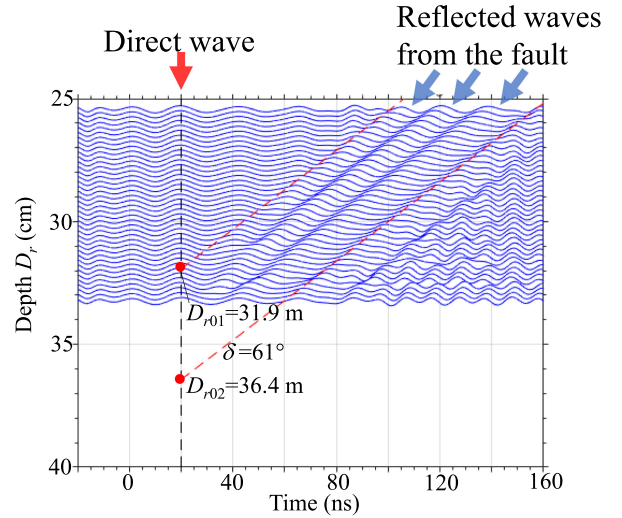


Fig. 7. CAB signals generated by the MoM after applying a time varying gain for amplitude compensation. The model is given in Fig. 5 with $\delta = 60^\circ$. The value of δ inside the figure is the estimated one.

paper [25]. In this method, two points were approximated by the calculation for fast computation. One was a far-field approximation of an electric field radiated by the dipole in [25 (31)]. The other was using the GO to compute the fields reflected from the interface, as referred to in [21 Sec. 13.2.3]. Although these two approximations enable us to calculate the reflected field very fast, if the antenna is close to the reflection point on the planar interface, the accuracy of the calculation is decreased. In this article, we show how to improve the calculation accuracy of the former approximation in the electric field radiated by the dipole in Appendix D. We confirm that our code of the MoM is valid in Appendix E. In this article, we replaced [25 (46)] with [26 (2.1.24)] to represent two layers of the planar interface unlike the one interface in [25]. We discuss the validity of the CRP (10) with the MoM calculation in Appendix F.

B. 3-D Imaging of a Planar Interface

We obtained the MoM data in the frequency domain in the manner of the previous section. We applied a band-pass filter (band-pass window centered at frequency $f_m = 47$ MHz) and the inverse discrete Fourier transform. The wavelength of the center frequency was about 1.6 m in the outermost layer. Fig. 7 shows the generated dipole array signals in the time domain. We applied the time varying gain [27] to compensate wave attenuation because of the wave loss in the medium. In the figure, we show one of the four dipole signals at depth D_r . A direct wave arrives at about 20 ns, after which oscillating signals remain. The half wavelength resonance of the transmitting dipole antenna causes the oscillations mainly. Reflected waves from the planar water layer reach the CAB after the direct wave. The antennas approach the intersection point at a depth of D_0 ; the reflected waves arrive earlier. We apply the proposed method to the data. First, we choose three peaks, indicated by the three blue arrows, to identify the reflected waves. We draw two red dotted lines, which follow the same phase of the reflected waves at each

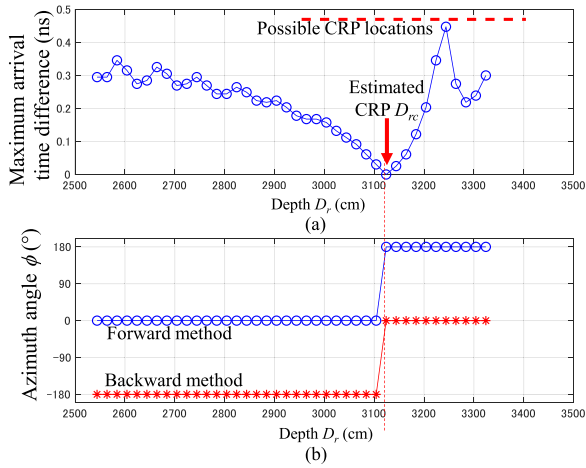


Fig. 8. Analysis of the CAB signals in Fig. 7. (a) Maximum arrival time difference. The horizontal bold dotted red bar shows the range of the possible CRP locations. (b) Estimated incident azimuth angle ϕ to the CAB. The true direction is 0° .

depth and surround the reflected waves. Seeing the intersections between the lines and the direct wave arrival time, indicated by the blue dotted line, the numerical values of D_{r01} and D_{r02} are chosen. Comparing the slope of the two lines and (1726), we estimate the dip angle δ . We calculate $z_{rc} = 3.9$ m with (10), the estimated δ , and the actual length d . We found the CEA to be $\theta_{rc} = 39^\circ$ according to similar analysis as in Fig. 14.

Fig. 8 shows the estimated MATD and DOA at each depth. We observed the series of waves from $(t, D_r) = (139 \text{ ns}, 2584 \text{ cm})$ to $(42 \text{ ns}, 3324 \text{ cm})$ in Fig. 7, and applied the DOA estimation method in Fig. 2. In the figure, we added the possible CRP locations determined from (12). From the depths of the possible CRP locations, we find that the MATD is minimum at a depth of 3124 cm in Fig. 8(a), and the estimated DOA changes rapidly at the same depth in Fig. 8(b). Therefore, we decide that this depth is the CRP D_{rc} . We choose the forward method for depths smaller than the CRP while adopting the backward method at a deeper region to determine the final value of the azimuth angle ϕ .

Fig. 9(a) and (b) shows the results of the 3-D estimation. In these figures, in order to represent the 3-D position of the reflection point and the normal vector \mathbf{n} , we introduce several small disks, equal in number to that of the datasets, as described in [15]. The center of each disk is at the estimated reflection point, and the normal vector of the disk is \mathbf{n} . The diameter of the disk is the same as the wavelength at the center frequency f_m . We added a white plane to represent the exact position of the planar interfaces, consisting of upper and lower boundaries. In Fig. 9(a), the positions of all the estimated disks are close to the white plane position. The inclinations of both the estimated disks and the white plane are almost the same. This result implies that the proposed method works well, although the dipole array antenna passed over the CRP. Using the conventional method, i.e., only using the forward method, we found that some disks were in the wrong direction, implying that the estimation failed.

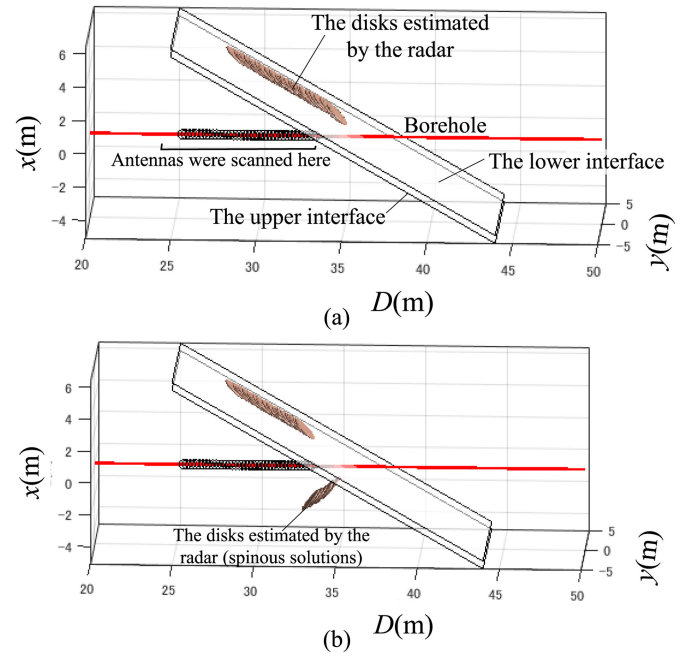


Fig. 9. 3-D images in the computer simulation. (a) Proposed method (forward method and backward method). (b) Conventional method (forward method only).

VI. FIELD EXPERIMENTS

In this section, we apply the proposed estimation method to the field measurement data of reflected waves from a fault. We have already reported the experimental field data acquired in the Kamioka mine in Japan and focused on a direct wave from a transmitting antenna to analyze antenna characteristics of the CAB in [13 Sec. III-D]. The site is composed of Hida gneiss. The horizontal borehole extends from the gallery to the rock in the test site. According to the boring cores acquired during the drilling, there are large fracture zones around the depth of $D = 43$ m, and the thickness of the zones is more than several meters. In fact, the wall surface of the horizontal borehole was too rough for the radar probe to enter depths deeper than $D_r = 36$ m. This fact may indicate that there is an interface in the fracture zone at the depths. In the present study, we analyze reflected waves from the fault rather than the direct wave. We set the CEA at 39° in this section by a similar manner as in Appendix B. The size of the horizontal borehole and the antennas are similar to the model in Fig. 5. Note that there is a centered conducting cylinder, which is a conducting housing over feed lines, near the CAB. We ignore this cylinder since we may ignore the cylinder's influence on the CAB signals [13]. The antennas are inside a vessel made of fiber reinforced plastics. We wrapped vinyl tapes around that vessel to center the radar probe inside the borehole. This centralizer ensures that the radar probe is in concentric cylindrical boundaries, like the model in Fig. 5. The sampled boring cores showed that the dip angle δ of the fault was about 60° . We assume in the estimation the relative permittivity of the rock to be 15.

Fig. 10 shows the time domain signals of one dipole element of the CAB. This figure and [13 Fig. 12] are from the same original

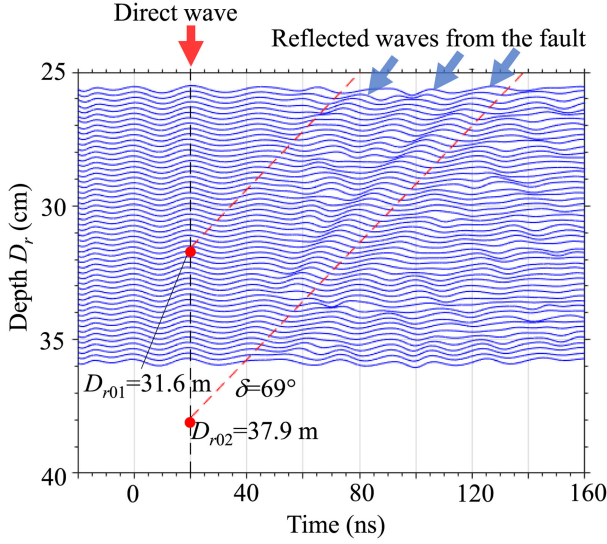


Fig. 10. Dipole array signals in the field experiment after applying a time varying gain for amplitude compensation. The value of δ inside the figure is the estimated one from the slope of the dotted red lines.

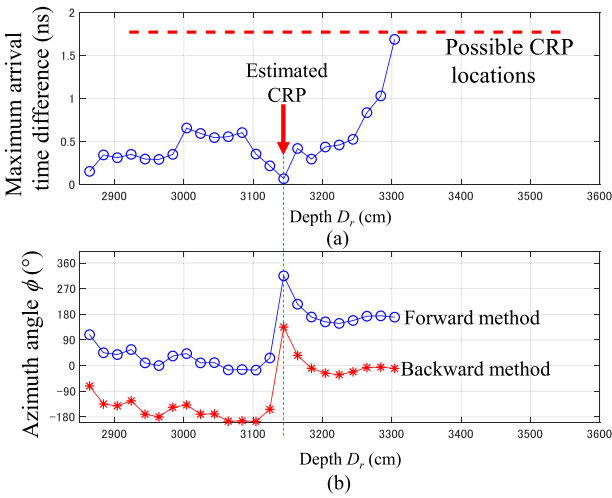


Fig. 11. DOA estimation results. (a) MATD. The horizontal bold dotted red bar shows the range of the possible CRP locations. (b) Estimated incident azimuth angle ϕ to the CAB. The true direction is about 0° .

data. The difference between the figures is that time varying gain has been applied in this article, but not previously. We can see direct waves around 20 ns at all positions. The reflected waves from the fault, indicated by the blue arrows, arrive after the direct wave. The time varying gain highlights the reflected wave in this figure, unlike in [13]. As in Section V-B, we draw two dotted red lines, on the peaks of the reflected waves and surround them. From the two intersections between the two lines and the direct wave's arrival, we determine the two values D_{r01} and D_{r02} . We estimate the dip angle δ from the slope of the two lines, as shown in Fig. 10.

In Fig. 11(a), the blue circles represent the measured MATD at each receiver position. For this estimation, we observed the series of waves from $(t, D_r) = (94 \text{ ns}, 2864 \text{ cm})$ to $(57 \text{ ns}, 3304 \text{ cm})$ in Fig. 10. We added the possible CRP locations

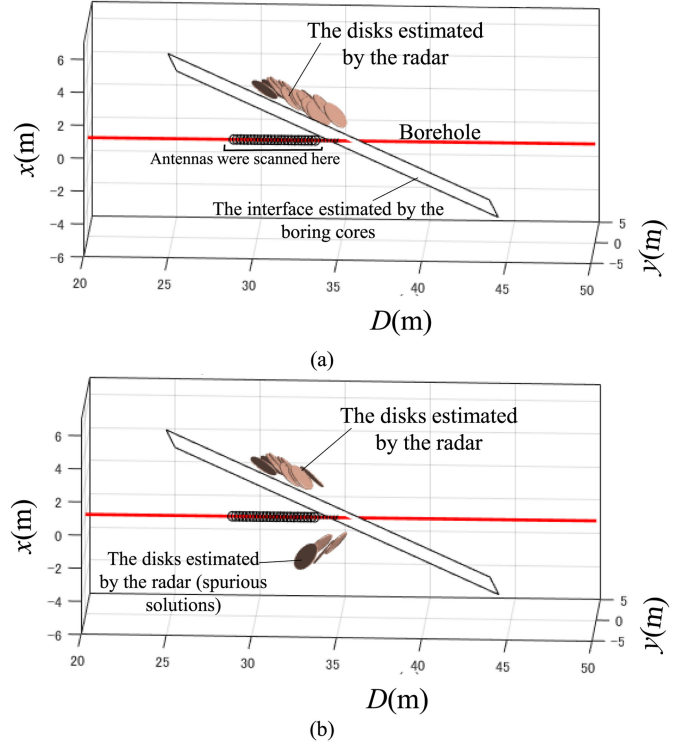


Fig. 12. 3-D images in the field experiment. The interface estimated by the boring cores at $D_0 = 35.2 \text{ m}$ is also shown. (a) Proposed method (The forward method and the backward method). (b) Conventional method (The forward method only).

between 2910 and 3540 cm, which we estimated from (10), (12), θ_{rc} , δ , D_{r01} , and D_{r02} . Fig. 11(b) shows the DOA estimation results with the forward method and backward method. We find minimization of the MATD and the rapid change of the incident azimuth angle ϕ at depths inside the possible CRP locations. This procedure determines the CRP, $D_{rc} = 31.44 \text{ m}$. According to some boring cores records, the azimuth angle ϕ of the reflected wave from the fracture zone should be about 0° . We find that the forward method yields almost correct azimuth angles ϕ between $D_r = 29.5 \text{ m}$ and 31 m , while the backward method gives accurate angles between $D_r = 32 \text{ m}$ and 33 m .

Fig. 12(a) and (b) shows the results of the 3-D estimation, where we utilized respectively the proposed method and only the forward method. All the disks are close to the white plane in Fig. 12(a), signifying that the proposed algorithm works well. There are two clusters in Fig. 12(b). Although one is close to the white plane, the other is in the opposite direction of the plane. This result means that the conventional method using only the forward method produces a spurious solution, as observed in the computer simulation.

VII. CONCLUSION

In this article, we have given one application example of phenomena discovered previously in the CAB. The phenomena are related to the CEP. We present an algorithm to create a 3-D image of a planar interface with the CAB directional borehole radar in situations where the antennas are close to the interface. With the

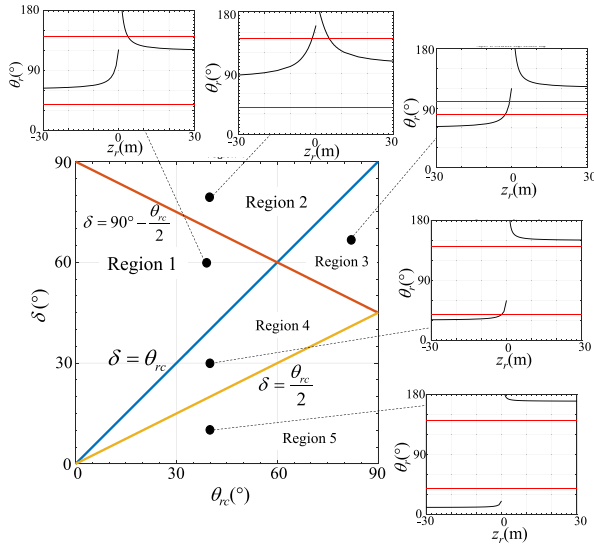


Fig. 13. CEA θ_{rc} and the dip angle δ of the interface. The point (θ_{rc}, δ) belongs to one of the five regions. The black curves in the five small graphs show examples of the angle θ_r versus the receiver position z_r in each region, and the horizontal red lines indicate the CEAs.

algorithm, we determine the MATE and the rapid change of the estimated DOA to obtain the CRP. Prior to this, we estimated this position roughly with possible CRP locations. We choose the forward method to estimate DOA at the positions where the CAB is far from the interface; we then choose the backward method after passing the CRP. According to the numerical simulations, we claim that there is a need to take into account the existence of the CRP in the case of an air-filled borehole in rock. We created a scenario where a planar water layer is near a borehole, and could successfully create a 3-D image of the interface of the layer. We then applied the proposed method to the field experimental data acquired at the Kamioka mine, Japan. The proposed algorithm could successfully generate a 3-D image of a fault near the actual position of the real fault, although the conventional algorithm was unsuccessful.

APPENDIX

A. Relationship Between the CEA and the Interface Dip Angle

Fig. 13 shows examples of graphs of θ_r on the $\theta_{rc}\delta$ plane. We may divide the $\theta_{rc}\delta$ plane into five regions. The three lines, which decide the existence of the intersection between the CEAs and θ_r , form the boundaries of the regions. The small five figures show examples of the curve for angle θ_r versus the receiver position z_r in each region. The CRP exists if the black curve intersects one of the red lines. As will be seen in Appendix B, the CEA may be less than about 40° in an actual borehole radar condition. Furthermore, we may expect to detect planar interfaces with the borehole radar with an approximate dip angle $30^\circ < \delta$ because of the dipole antenna's radiation pattern. This assumption may agree with the detected fractures in [6]. The information abovementioned suggests that we should concentrate our attention on the case where (θ_{rc}, δ) is in regions 1 or 2. We add our comments on each case as follows.

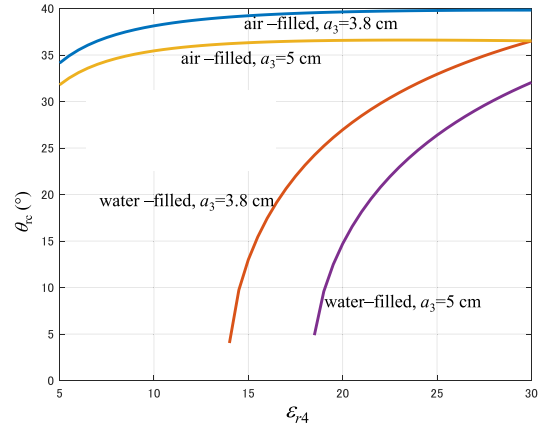


Fig. 14. Dependence of the critical elevation angles θ_{rc} on the relative permittivity ϵ_{r4} of the outermost layer. The frequency is 100 MHz. The relative permittivity of the third layer is $\epsilon_{r3} = 1$ for the air-filled borehole and $\epsilon_{r3} = 80$ for the water-filled borehole. The other used parameters are $2a_1 = 4.4$ cm, $2a_2 = 5.4$ cm, $\epsilon_{r1} = 1$, $\epsilon_{r2} = 5$, $2h_r = 20$ cm, and $2b = 4$ cm in Fig. 1.

Region 1: This case corresponds to the situation in Fig. 4. Here, we may always apply the forward method when the antennas are under the interface since the incident elevation angle θ_r is at the range $\theta_{rc} < \theta_r < 180^\circ - \theta_{rc}$. However, we apply the backward method instead of the forward method only when the antennas are above and close to the interface. We propose this procedure in Section IV.

Region 2: We need to apply the backward method if the antennas are close to the interface despite the ambiguous relationship between the antennas and the interface. However, it seems to be most important to consider the existence of the CRP in (10) when the signals of the CAB are processed. This is because of the limited receiver positions where the CAB is under the interface, and we should apply the backward method.

Region 3–5: It seems that such situations rarely occur in actual borehole radar measurements since the CEA needs to be more than about 40° .

B. Dependency of CEA on Permittivity in Outermost Layer

Fig. 14 shows the dependency of the CEA on the permittivity of the outermost layer. We calculated the azimuthal dependence criterion of [20] (10), and determined the CEA. If the outermost layer is a rock, the relative permittivity may range between about 5 to 15 [27]. In this case, the existence of CEA in the water-filled boreholes may be ignored since the CEA disappears in the figure. However, if the borehole is filled with air and the outermost layer is rock, we find that the CEA is more than 35° and, thus, the existence of the CEA needs to be considered more carefully. One example of an air-filled borehole in rock is a horizontal borehole drilled from a gallery, where the proposed algorithm in Section IV, in this article, may play an important role. If the outermost layers are wet soil, it is assumed that the relative permittivity is larger than about 20. In this case, we need to take into account the existence of the CEA even if the borehole is filled with water.

C. Slope of Reflected Wave Arrival Time in Radargram

We consider the coordinate system (ρ, z) in Fig. 3. The total distance of the line from the transmitter to the receiver via the variable point $(\rho, \rho \tan \delta)$ on the planar interface is given by

$$f(\rho, z_r) = \sqrt{\rho^2 + (\rho \tan \delta - z_r + d)^2} + \sqrt{\rho^2 + (\rho \tan \delta - z_r)^2}. \quad (13)$$

When the variable point $(\rho, \rho \tan \delta)$ matches the reflection point (ρ_s, z_s) of the specular reflection, the equation

$$\left. \frac{\partial f(\rho, z_r)}{\partial \rho} \right|_{\rho=\rho_s} = 0 \quad (14)$$

is established. Solving the above equation, we determine

$$\rho_s = \frac{z_r(d - z_r) \sin 2\delta}{d - 2z_r} \quad (15)$$

and

$$z_s = \frac{z_r(d - z_r) \sin 2\delta}{d - 2z_r} \tan \delta. \quad (16)$$

The slope of the straight line drawn on the graph, whose horizontal axis is the arrival time t and vertical axis is the receiver position z_r , is

$$\frac{v}{g(\delta)} \text{ [m/s]} \quad (17)$$

where

$$g(\delta) = \lim_{z_r \rightarrow \infty} \frac{\partial f(\rho_s, z_r)}{\partial z_r} = \frac{2(1 - \sin^2 \delta)}{\sqrt{1 - \sin^2 \delta}}. \quad (18)$$

The constant v is the plane wave velocity in the outermost layer of the cylindrical layers in Fig. 1. Note that, if the vertical axis is the receiver position D_r instead of z_r , we need to use the negative value of (17).

D. Electric Field Radiated by a z -Directed Dipole in a Borehole

Hansen determined the received electric field at the center of a borehole in the case where the borehole is in the vicinity of a planar interface. The theory is based on the principle of a mirror image. In his study, the source is a vertical electric Hertzian dipole at the center of the borehole, where the number of the cylindrical layers is two. Hansen utilized the far-field approximation of the saddle point contribution of [25 (31)] for fields radiated by the source. Alternatively, in this article, we introduced the following exact solution of the fields. Consider the vertical electric Hertzian dipole at (ρ', ϕ', z') in the innermost layer in cylindrical layers, as shown in Fig. 15. Referring to [28 (13)], we obtain the saddle-point contribution component of the electromagnetic field (E_{Nz}, H_{Nz}) at (ρ, ϕ, z) in the outermost layer by integration along the steepest descent path as

$$\begin{bmatrix} E_{Nz} \\ H_{Nz} \end{bmatrix} = \frac{iIl}{4\pi\omega\epsilon_1} \sum_{n=-\infty}^{\infty} e^{in(\phi-\phi')} e^{rh(k_{z0})}$$

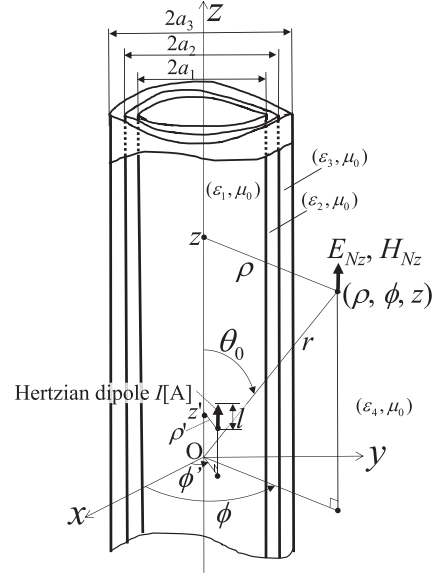


Fig. 15. Vertical electric Hertzian dipole in cylindrical layers. The value of ϵ_i is the relative complex permittivity in the i th layer.

$$\times \int_{-\infty}^{\infty} e^{-rs^2} f(k_z) \frac{dk_z}{ds} ds \quad (19)$$

where

$$-s^2 = h(k_z) - h(k_{z0}) \quad (20)$$

$$h(k_z) = ik_z \cos \theta_0 + ik_{N\rho} \sin \theta_0 \quad (21)$$

$$k_{N\rho 0} = k_N \sin \theta_0, k_{z0} = k_N \cos \theta_0 \quad (22)$$

$$z - z' = r \cos \theta_0, \rho = r \sin \theta_0 \quad (23)$$

$$r = \sqrt{\rho^2 + (z - z')^2} \quad (24)$$

$$f(k_z) = e^{-ik_{N\rho}\rho} H_n^{(1)}(k_{N\rho}\rho) J_n(k_{1\rho}\rho') \tilde{\mathbf{T}}_{1,N}^{(n)} \left[k_{1\rho}^2 \right]. \quad (25)$$

In the abovementioned equations, the value $k_{i\rho}$ is given by $k_{i\rho} = \sqrt{k_i^2 - k_z^2}$ ($i = 1, 2, \dots, N$), where k_i is the wavenumber of a plane wave in the i th layer, and k_z is the z -component of the wavenumber in all regions. The 2×2 matrix $\tilde{\mathbf{T}}_{1,N}^{(n)}$ is a transmission matrix of the n th order from the innermost layer to the N th layer in [26 (3.2.11a)]. The notation $|\cdot|^{(1)}$ means the value at the cell in the first row of the vector inside the round bracket. The spherical component of the radiated field from the source is

$$E_\theta = E_{N\rho} \cos \theta_0 - E_{Nz} \sin \theta_0 \quad (26)$$

where

$$E_{N\rho} = \frac{1}{k_{N\rho}^2} \left(ik_z \frac{\partial}{\partial \rho} E_{Nz} - \frac{n\omega\mu_0}{\rho} H_{Nz} \right) \quad (27)$$

which is from [26 (3.1.4a)]. We used (26) with (19) in this article, instead of [25 (31)]. We should notice that utilizing the MATLAB command “quadgk” helps fast and accurate evaluation of the numerical integration in (26).

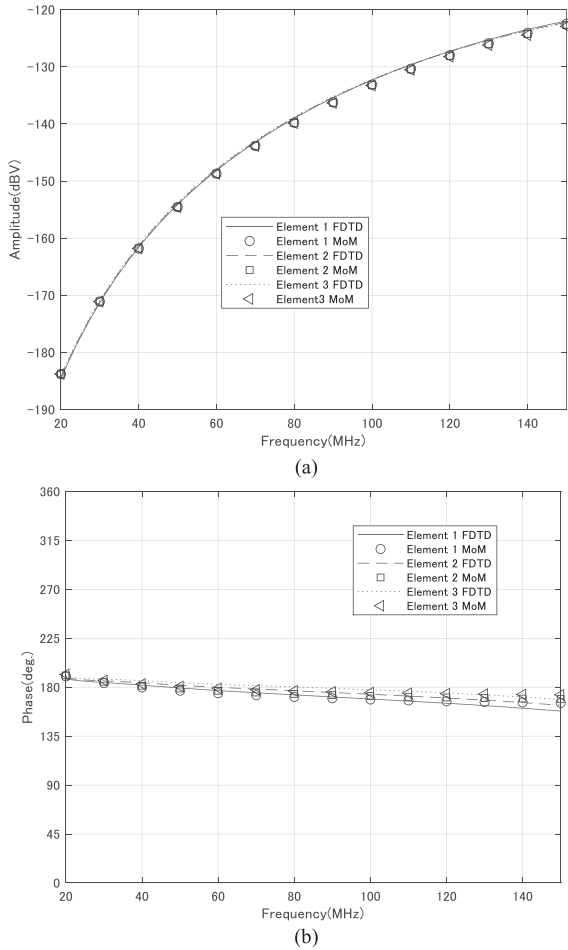


Fig. 16 Comparison between FDTD and MoM. The model parameters in Fig. 5 are $d = 1.5$ m, $D_0 = 35$ m, $D_r = 31.2$ m, $\delta = 50^\circ$, $w = 0.1$ m, $2a_1 = 4.4$ cm, $2a_2 = 5.4$ cm, $2a_3 = 7.6$ cm, $\epsilon_{r1} = 1$, $\epsilon_{r2} = 5$, $\epsilon_{r3} = 1$, $\epsilon_{r4} = 15 - j(1 \times 10^{-2} \text{ S/m})/(\epsilon_0 \omega)$, $\epsilon_r = 30$, $2h_r = 2h_t = 20$ cm, $2a_t = 2$ mm, and $2b = 4$ cm. (a) Amplitude. (b) Phase.

E. Verification of the MoM Signal With FDTD

A commercial software package, Poynting for Microwave (Fujitsu Ltd.), was used to obtain the finite difference time domain (FDTD) [29] values. A perfect matched layer technique was used to construct an absorbing boundary. The Cartesian dimensions for the FDTD simulation were $9 \times 9 \times 9$ m. Nonuniform orthogonal grids were used, and the finest cell discretization size was 1 mm in the region around the feed point. The excitation pulse at the source was a Gaussian pulse modulated at 60 MHz. We applied a fast Fourier transform to both the excitation voltage pulse and the detected voltage at the feeding point of the receiving dipole element. We divided the observed voltage value by the excitation voltage pulse value in the frequency domain and calculated a transfer function between the excitation and observed voltages. The GO approximation analysis in (15) assumes that there is a reflection point, $\rho_s = 1.5$ m far from the borehole in the simulated case. Fig. 16 shows the amplitude and phase of the transfer functions obtained with the FDTD and calculated by the MoM used in this article. We find that the MoM values show agreement with the FDTD values.

F. Error of Calculation of Reflection at a Planar Interface

It is important to understand the accuracy of (10), which we derived by assuming the GO approximation, the point source, and the small receiver. In an actual radar measurement, the antennas have a finite size. Furthermore, the distance between the antennas and the planar interface is relatively short compared with the wavelength. In this appendix, we verify the accuracy of (10) with the MoM data. Since the approximation error in even in the MoM remains, we evaluate the MoM value accuracy first and then compare the values of (10) with the ones calculated by the MoM.

Despite the replacement of [25 (31)] with (26) in this article, the image theory approximation in the reflection given in [25 (51)] remains. In the principle of the image theory, the Fresnel reflection coefficients at a single reflection point represent total reflection. This assumption is perfectly accurate when the planar interface is a perfect conductor. However, if the planar interface is a lossy dielectric, the assumption is not valid since the Fresnel reflection coefficients depend on the wave's incident angle to the planar interface. Especially, the approximation gets worse at steep oblique incidence to the interface. We introduce a criterion to quantify the error of the reflection at the interface using the method in [25], as follows. The calculation of the electromagnetic fields in the borehole radar measurement of the planar interface corresponds to that in the situation where there is a point source above the top of a planarly layered medium when the borehole does not exist. We may calculate this electromagnetic field exactly with the [26 (2.3.5), (2.3.9), and (2.3.17)]. We define this electric field obtained from the exact solution with the source above the planarly layered media as E'_z . On the other hand, we may calculate the field obtained by the image theory solution in [25 (51)] when the borehole does not exist. We define this value as E_z . The error of the image theory may be defined as

$$\text{error} = 20 \log_{10} \left| \frac{E_z - E'_z}{E'_z} \right| \quad [\text{dB}]. \quad (28)$$

The black curve in Fig. 17 is the dependency of the CRP calculated by (10). The red and blue curves are the MoM solutions. We may generate the time domain signals of the CAB and estimate the CRP in the same way as in Fig. 8. The difference between the CRP D_{rc} and the real intersection position D_0 may provide the output z_{rc} of the MoM. We have added the contours of the error magnitude in Fig. 17. These contours describe the reliability of the two MoM curves at each point on the $\delta - z_{rc}$ plane. As the dip angle becomes large, the reflection point gets close to the antennas. This fact leads to a steep oblique incidence of the electromagnetic wave on the planar interface, which may increase the error of the MoM data. When the dip angle is lower than about 60° , the error magnitude becomes lower than -30 dB, and the MoM curves at the dip angles are reliable. In this range, we find the CRP values of (10) are close to those of the MoM. We may conclude that the CRP in (10) works well in the rough estimation of the CRP location, regardless of the length of the transmitter.

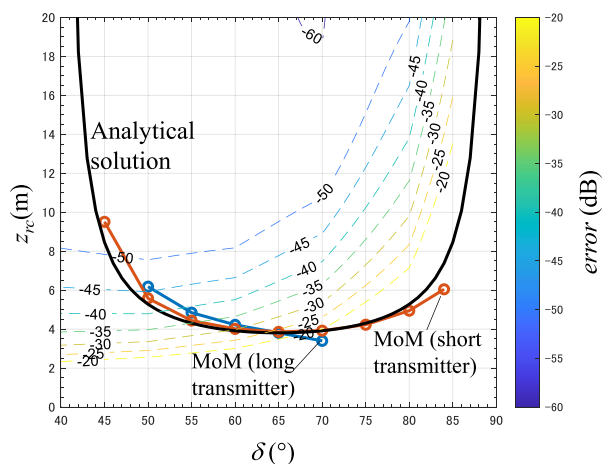


Fig. 17. Dependence of the critical elevation angles. Equation (10) gives an “Analytical solution.” The MoM with the model in Fig. 5 outputs “MoM (long transmitter),” while the MoM with the model in Fig. 5 except for $2h_t = 0.2$ m and $2a_t = 2$ mm outputs “MoM (short transmitter).” The contour shows the value, which (28) outputs to represent the accuracy of the image theory solution in the MoM.

ACKNOWLEDGMENT

The authors would like to thank Kamioka Mining & Smelting Company, Ltd. for full support in doing experiments in Kamioka mine in October 2012, and also like to thank Prof. J. Yamatomi from the University of Tokyo, K. Saeki from Okuaizu Geothermal Company, Ltd., K. Yamanaka from Mitsui Mining & Smelting Company, Ltd., and K. Wada from Mitsui Mineral Development Engineering Company, Ltd. for kind comments in planning the field experiments.

REFERENCES

- [1] J. Wang, L. Chen, R. Su, and X. Zhao, “The Beishan underground research laboratory for geological disposal of high-level radioactive waste in China: Planning, site selection, site characterization and in situ tests,” *J. Rock Mech. Geotechnical Eng.*, vol. 10, pp. 411–435, 2018.
- [2] S. Torata, K. Fukuoka, T. Sugiyama, K. Yoshimura, J. Ohuchi, and T. Tsuboya, “Monitoring of geological disposal - current status and technical possibilities -,” RWMC-TRE-04004, 2005.
- [3] T. Yamamoto, S. Shirasagi, Y. Yokota, and Y. Koizumi, “Imaging geological conditions ahead of a tunnel face using three-dimensional seismic reflector tracing system,” *Int. J. JCRM*, vol. 6, no. 1, pp. 23–31, 2010.
- [4] L. Liu, “Fracture characterization using borehole radar: Numerical modeling,” *Water, Air, Soil Pollution, Focus*, vol. 6, pp. 17–34, 2006.
- [5] F. Zhou, M. Mattia, S. Evert, and H. Xiangyun, “Reservoir monitoring using borehole radars to improve oil recovery: Suggestions from 3D electromagnetic and fluid modeling,” *Geophysics*, vol. 83, no. 2, pp. WB19–WB32, 2018.
- [6] S. Liu and M. Sato, “Subsurface water-filled fracture detection by borehole radar: A case history,” *J. Environ. Eng. Geophys.*, vol. 11, no. 2, pp. 95–101, 2006.
- [7] C. Ma, Q. Zhao, L. Ran, and X. Chang, “Numerical study of borehole radar for cliff imaging,” *J. Environmental Eng. Geophys.*, vol. 19, no. 4, pp. 269–276, 2014.
- [8] C. Ma, Q. Zhao, J. Huo, X. Chang, and L. Ran, “Single borehole radar for well logging in a limestone formation: experiments and simulations,” *J. Environmental Eng. Geophys.*, vol. 21, no. 4, pp. 201–213, 2016.
- [9] L. Mao and B. Zhou, “Simulation and analysis of conductively guided borehole radar wave,” *IEEE Trans. Geosci. Remote Sens.*, vol. 55, no. 5, pp. 2646–2657, May 2017.
- [10] J. Huo, Q. Zhao, L. Liu, C. Ma, J. Guo, and L. Xie, “Energy flow domain reverse-time migration for borehole radar,” *IEEE Trans. Geosci. Remote Sens.*, vol. 57, no. 9, pp. 7221–7231, Sep. 2019.

- [11] S. Ebihara, “Directional borehole radar with dipole antenna array using optical modulators,” *IEEE Trans. Geosci. Remote Sens.*, vol. 42, no. 1, pp. 45–58, Jan. 2004.
- [12] M. Sato and T. Takayama, “A novel directional borehole radar system using optical electric field sensors,” *IEEE Trans. Geosci. Remote Sens.*, vol. 45, no. 8, pp. 2529–2535, Aug. 2007.
- [13] S. Ebihara, Y. Kimura, T. Shimomura, R. Uchimura, and H. Choshi, “Coaxial-fed circular dipole array antenna with ferrite loading for thin directional borehole radar sonde,” *IEEE Trans. Geosci. Remote Sens.*, vol. 53, no. 4, pp. 1842–1854, Apr. 2015.
- [14] T. Takayama and M. Sato, “A novel direction-finding algorithm for directional borehole radar,” *IEEE Trans. Geosci. Remote Sens.*, vol. 45, no. 8, pp. 2520–2528, Aug. 2007.
- [15] S. Ebihara, H. Kawai, and K. Wada, “Estimating 3-D position and inclination of a planar interface with directional borehole radar,” *Near Surface Geophys.*, vol. 11, pp. 185–195, 2013.
- [16] S. Liu, W. Wang, L. Fu, and Q. Lu, “Linear prediction-based DOA estimation for directional borehole radar 3-D imaging,” *IEEE Trans. Geosci. Remote Sens.*, vol. 57, no. 8, pp. 5493–5501, Aug. 2019.
- [17] S. Ebihara, K. Wada, S. Karasawa, and K. Kawata, “Probe rotation effects on direction of arrival estimation in array-type directional borehole radar,” *Near Surface Geophys.*, vol. 15, no. 3, pp. 286–297, 2017.
- [18] A. M. Badescu, “The transfer function of a boreholed dipole antenna,” *IEEE Trans. Antennas Propag.*, vol. 66, no. 11, pp. 5757–5763, Nov. 2018.
- [19] J. Cho, J. Jung, S. Kim, and S. Kim, “Suppression of borehole-guided waves supported by the connection cable of a single-borehole monostatic pulse radar,” *IEEE Trans. Geosci. Remote Sens.*, vol. 51, no. 6, pp. 3431–3438, Jun. 2013.
- [20] S. Ebihara, S. Kotani, and K. Fujiwara, “Arrival times of plane waves obliquely incident on a dipole array antenna in a borehole,” *IEEE Trans. Geosci. Remote Sens.*, vol. 58, no. 5, pp. 3273–3286, May 2020.
- [21] C. Balanis, *Advance Engineering Electromagnetics*, New York, NY, USA: Wiley, 1989.
- [22] S. Ebihara, K. Wada, S. Karasawa, and K. Kawata, “Probe rotation effects on direction of arrival estimation in array-type directional borehole radar,” *Near Surface Geophys.*, vol. 15, pp. 286–297, 2017.
- [23] S. Liu and M. Sato, “Electromagnetic logging technique based on borehole radar,” *IEEE Trans. Geosci. Remote Sens.*, vol. 40, no. 9, pp. 2083–2092, Sep. 2002.
- [24] R. F. Harrington, *Field Computation by Moment Methods*, Piscataway, NJ, USA: Wiley, 1993.
- [25] T. B. Hansen, “The far field of a borehole radar and its reflection at a planar interface,” *IEEE Trans. Geosci. Remote Sens.*, vol. 37, no. 4, pp. 1940–1950, Jul. 1999.
- [26] W. C. Chew, *Waves and Field in Inhomogeneous Media*, New York, NY, USA: IEEE, 1995.
- [27] D. Daniels, *Ground Penetrating Radar*, 2nd ed. London, U.K.: IEE, 2004.
- [28] S. Ebihara and Y. Hashimoto, “MoM analysis of dipole antennas in crosshole borehole radar, and field experiments,” *IEEE Trans. Geosci. Remote Sens.*, vol. 45, no. 8, pp. 2435–2450, Aug. 2007.
- [29] A. Taflov and S. C. Hagness, *Computational Electrodynamics: The Finite-Difference Time-Domain Method*, Norwood, MA, USA: Artech House, 2005.



Satoshi Ebihara (Member, IEEE) was born in Chiba, Japan, in December 10, 1968. He received the B.S., M.S., and Dr. Eng. degrees in resources engineering from Tohoku University, Sendai, Japan, in 1993, 1995, and 1997, respectively.

From 1995 to 1997, he was a Research Fellow with the Japan Society for the Promotion of Science, Tokyo, Japan. From 1997 to 2003, he was a Research Associate with the Center for Northeast Asian Studies, Tohoku University. In 2003, he joined Osaka Electro-Communication University (OECU),

Neyagawa, Japan, and he is currently a Professor with the Department of Electrical and Electronic Engineering, Faculty of Engineering, OECU. His current research interest includes borehole radar measurement.

Dr. Ebihara was the recipient of several awards, including the Best Reviewer Award from the IEEE TRANSACTIONS ON GEOSCIENCE AND REMOTE SENSING, in 2016, the Young Researchers Award from the Miyagi Foundation for Promotion of Industrial Science, Sendai, Japan, in March 2001, and the Best Paper Award from the Second Well-Logging Symposium of Japan, Chiba, Japan, in September 1996.



Shyuhei Kotani was born on May 18, 1995. He received the B.S. degree in electrical and electronic engineering from Osaka Electro-Communication University, Neyagawa, Japan, in 2018.

He is currently with Kurihara Kogyo Company, Ltd., Japan.



Takaaki Shimomura was born on July 3, 1989. He received the B.S. degree in electrical and electronic engineering from Osaka Electro-Communication University, Neyagawa, Japan, in 2013.

He is currently with West Nippon Expressway Engineering Kansai Company Ltd., Japan.



Kengo Fujiwara was born on October 28, 1995. He received the B.S. degree in electrical and electronic engineering from Osaka Electro-Communication University, Neyagawa, Japan, in 2018.

He is currently with Mitsubishi Electric Building Techno Service Company, Ltd., Japan.



Ryota Uchimura was born on September 24, 1990. He received the B.S. degree in electrical and electronic engineering from Osaka Electro-Communication University, Neyagawa, Japan, in 2013.

He is currently with Kanden Engineering Corporation, Japan



Yuta Kimura was born on February 12, 1991. He received the B.S. degree in electrical and electronic engineering from Osaka Electro-Communication University, Neyagawa, Japan, in 2013.

He is currently with Kinden Corporation, Japan.